Stiffness Compensation Through Matching Buckling Loads in a Compliant Four-Bar Mechanism

Numic, A.; Blad, T. W.A.; van Keulen, F.

DOI
10.1115/1.4052333

Publication date
2022

Document Version
Final published version

Published in
Journal of Mechanisms and Robotics

Stiffness Compensation Through Matching Buckling Loads in a Compliant Four-Bar Mechanism

A. Numić
Department of Precision and Microsystems Engineering,
Delft University of Technology,
Delft 2628 CD, The Netherlands
e-mail: a.numic@vu.nl

T.W.A. Blad[1]
Department of Precision and Microsystems Engineering,
Delft University of Technology,
Delft 2628 CD, The Netherlands
e-mail: t.w.a.blad@tudelft.nl

F. van Keulen
Department of Precision and Microsystems Engineering,
Delft University of Technology,
Delft 2628 CD, The Netherlands
e-mail: a.vankeulen@tudelft.nl

In this paper, a novel alternative method of stiffness compensation in buckled mechanisms is investigated. This method involves the use of critical load matching, i.e., matching the first two buckling loads of a mechanism. An analytical simply supported five-bar linkage model consisting of three rigid links, a prismatic slider joint, and four torsion springs in the revolute joints is proposed for the analysis of this method. It is found that the first two buckling loads are exactly equal when the two grounded springs are three times stiffer than the two ungrounded springs. The force–deflection characteristic of this linkage architecture showed statically balanced behavior in both symmetric and asymmetric actuation. Using modal analysis, it was shown that the sum of the decomposed strain energy per buckling mode is constant throughout the motion range for this architecture. An equivalent lumped-compliant mechanism is designed; finite element and experimental analysis showed near-zero actuation forces, verifying that critical load matching may be used to achieve significant stiffness compensation in buckled mechanisms. [DOI: 10.1115/1.4052333]

Keywords: compliant mechanisms, mechanism design, mechanism synthesis, static balancing, buckling

1 Introduction

A statically balanced mechanism is in static equilibrium at every point over a finite range of motion. In this case, the total potential energy of the mechanism is constant [1]. Static balancing may for instance be used to compensate for the gravity load of a mechanism. Not only gravity loads but also elastic energy stored during deformation such as in compliant mechanisms (CMs) can be balanced. As a result, the force required for this deformation is zero [2].

A frequently used method to achieve static balancing in, for example, linkages is an intricate synthesis of ideal springs and auxiliary rigid bodies [3–6]. The springs are responsible for counteracting undesired forces occurring during deflection. In CMs, strain energy accumulates in the elastic elements due to their inherent positive stiffness [7]. Static balancing in CMs is achieved through stiffness compensation, i.e., cancelation of the positive stiffness using equal but negative stiffness [8]. This negative stiffness is introduced through pre-loading of elastic elements. Accumulated strain energy is compensated by the energy stored in the pre-loaded elements during the deformation [9]. As a result, the net change in energy is small; hence, the required input force reduces [10–12].

Current methods of stiffness compensation require an iterative process of finding the correct negative stiffness and force–deflection (FD) characteristics [13,14], or geometrical optimization [2,15,16,17]. Kuppens et al. [18] introduced a novel notion on using pre-loading in stiffness compensation of CMs. In this work, the stiffness of a mechanism is minimized by matching the first two critical buckling loads. Blad et al. [19] defined the ratio between these buckling loads as the critical load ratio (CLR), which is used to identify the variation of potential energy between the equilibria of the buckled mechanism in question. The CLR was applied as a strategy to balance several orthoplanar CMs, and the effect of geometrical parameters on the mechanical behavior was investigated. It was shown that by maximizing this ratio, i.e., matching the two buckling loads, a minimal actuation force is obtained in transversal deflection. This method may be a simple alternative for stiffness compensation in designing statically balanced CMs. However, the working of this method has yet to be applied to lumped-compliant mechanisms for, e.g., stiffness compensation in linkages.

In this research, the use of the CLR as a means of stiffness compensation is investigated. The goal of this paper is to provide analytical substantiation for the use of the CLR to achieve stiffness compensation. Additionally, this method is numerically and experimentally verified using a new mechanism design.

In Sec. 2, the concept of stiffness compensation using the CLR is presented. Subsequently, an analytical framework using a five-bar linkage with torsion springs is formed. The buckling problem for this analytical model is solved, the CLR is established, and modal analysis of the deformation is discussed. Additionally, the mechanical design of an equivalent lumped-compliant mechanism, finite element modeling, and the experimental setup are covered. In Sec. 3, the results obtained from the analytical, finite element, and experimental analyses are presented. Section 4 discusses these results and concluding remarks are given in Sec. 5.

2 Methods

2.1 Buckling of Five-Bar Linkage. Buckling is feared in engineering due to the danger of catastrophic failure of structures [20]. When several buckling loads are close together, a phenomenon defined as buckling mode interaction, this danger grows significantly larger [21]. In this research, however, exactly this phenomenon is used for stiffness compensation in a five-bar linkage. Figure 1 displays a schematic representation of this five-bar linkage, consisting of three links, four revolute joints, and a prismatic slider joint. Its flat configuration in Fig. 1(*a*) is a stable equilibrium which is defined as the pre-buckling state [22]. The slider joint allows for axial pre-loading through, e.g., an axial load P. During pre-loading, the axial load P is gradually increased while the linkage preserves its flat configuration, up to the point that it holds $P = P_{cr,1}$. Eventually, the linkage deflects transversally in, e.g., the gray buckled configuration. Its FD behavior may now be evaluated by imposing an external load F in an arbitrary location and deflecting the linkage in the y-direction.

$P_{cr,1}$ is the first critical buckling load, i.e., the lowest axial load at which the pre-buckling state loses stability, and bifurcates into a

[1]Corresponding author.

Contributed by Mechanisms and Robotics Committee of ASME for publication in the Journal of Mechanisms and Robotics. Manuscript received March 14, 2021; final manuscript received August 24, 2021; published online September 21, 2021. Assoc. Editor: Guimin Chen.

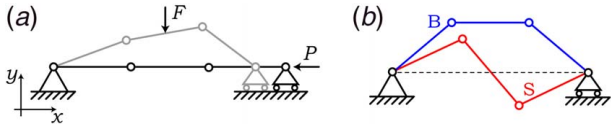

Fig. 1 Schematic representation of five-bar linkage in (*a*) flat and buckled state and (*b*) its two buckling modes. As a result of axial load *P*, the linkage buckles from the flat into the deformed (gray) configuration from which it may be transversally deflected using an external load *F*. The linkage has two buckling modes: (—) the B-mode, and (—) the S-mode.

new equilibrium that is called the post-buckling state [23]. Figure 1(*b*) displays the possible post-buckling equilibria of the linkage, which are the two buckling modes. These are defined as the B and S-modes, as the linkage forms a bridge and S-shape, with their corresponding critical buckling loads P_B and P_S, respectively. The CLR, i.e., the ratio of these two buckling loads, describes the variation of potential energy between the equilibrium states of a buckled mechanism [19]. During transversal deflection, the linkage will transition between these equilibrium states. By achieving a unity CLR, the two buckling loads, and thus the potential energies in the equilibria, are equal. As a result, constant potential energy between the equilibria, and hence static balancing, is obtained. This effect is visualized with the strain energy contributions of the B and S-modes under transversal deflection using modal analysis in Sec. 2.2.4. A more practical visualization is by means of the FD characteristic of the linkage under transversal deflection, as described in Sec. 2.2.

2.2 Analytical Framework. To use the CLR as a method for stiffness compensation, the buckling loads and modes of the linkage have to be obtained. Figure 2 displays the proposed model of the torsion spring linkage (TSL) used in this analysis. The TSL consists of three rigid links of length L; a prismatic slider joint; and four torsion springs in the revolute joints with stiffness k_a, k_b, k_c, and k_d, which capture the elastic properties of the linkage. Additionally, a spring with stiffness k in the axial direction, connected to the prismatic slider joint, functions as the pre-loading mechanism: by displacing the frame connection a distance d in the x-direction, the linkage is loaded axially and brought into post-buckling. The five-bar linkage allows for two degrees of freedom (DoFs) as a description of the kinematics, which are chosen as $\mathbf{u} = [\varphi_1,\ \varphi_2]^T$. The resulting stiffness compensation is evaluated by means of the FD characteristic of the TSL under deflection in the y-direction. To this end, two external loads, an asymmetric load F_a and symmetric load F_s, are imposed in O_a and O_s, respectively.

2.2.1 Kinematics. Figure 3 presents the kinematics of a single link. Its displacement in the horizontal and vertical directions is described by the change in endpoint displacements and can be found in Eqs. (1) and (2). These displacements are simplified by

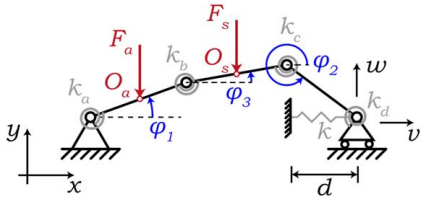

Fig. 2 Schematic representation of the torsion spring linkage. The kinematics are described by the two degrees of freedom $\mathbf{u} = [\varphi_1,\ \varphi_2]^T$. By applying a pre-loading displacement *d* to the rigid connection of spring *k*, the linkage is brought into a buckled state in which an asymmetric load F_a and symmetric load F_s are imposed in O_a and O_s, respectively.

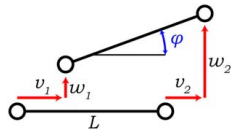

Fig. 3 Kinematics of a single link, consisting of horizontal displacement *v*, vertical displacement *w* and rotation φ

assuming moderate rotations ($\varphi^2 \ll 1$).

$$\Delta v = v_2 - v_1 = L(\cos\varphi - 1) \approx -\frac{1}{2}L\varphi^2 \tag{1}$$

$$\Delta w = w_2 - w_1 = L\sin\varphi \approx L\varphi \tag{2}$$

The horizontal and vertical displacements of the prismatic slider joint are found by summing Eqs. (1) and (2), respectively, for the angles φ_1 to φ_3. As a result of the slider joint, it follows that $w = 0$, which allows for a description of the five-bar linkage kinematics in terms of the DoFs $\mathbf{u} = [\varphi_1, \varphi_2]^T$ as found in Eqs. (3) and (4)

$$\varphi_3 = -\varphi_1 - \varphi_2 \tag{3}$$

$$v = -L\left(\varphi_1^2 + \varphi_1\varphi_2 + \varphi_2^2\right) \tag{4}$$

2.2.2 Buckling Problem. The buckling problem is solved using the energy approach [24], which will return the bifurcation buckling loads and corresponding modes. To this end, the potential energy Φ of the TSL is established as found in Eq. (5)

$$\begin{aligned}\Phi[\varphi_1;\varphi_2;\varphi_3;d;v;F_a;F_s] = &\frac{1}{2}k_a\varphi_1^2 + \frac{1}{2}k_b(\varphi_3-\varphi_1)^2 \\ &+\frac{1}{2}k_c(\varphi_2-\varphi_3)^2 + \frac{1}{2}k_d\varphi_2^2 \\ &+\frac{1}{2}k(d-v)^2 + \frac{1}{2}F_aL\varphi_1 \\ &+L\left(\varphi_1+\frac{1}{2}\varphi_3\right)F_s\end{aligned} \tag{5}$$

The potential energy is expressed in terms of the DoFs $\mathbf{u}$ using Eqs. (3) and (4) and can be found in Eq. (6)

$$\begin{aligned}\Phi[\mathbf{u};d;F_a;F_s] = &\frac{1}{2}k_a\varphi_1^2 + \frac{1}{2}k_b(2\varphi_1+\varphi_2)^2 + \frac{1}{2}k_c(\varphi_1+2\varphi_2)^2 \\ &+\frac{1}{2}k_d\varphi_2^2 + \frac{1}{2}k\left[d+L\left(\varphi_1^2+\varphi_1\varphi_2+\varphi_2^2\right)\right]^2 \\ &+\left(\frac{1}{2}F_aL+\frac{1}{2}F_sL\right)\varphi_1 - \frac{1}{2}F_sL\varphi_2\end{aligned} \tag{6}$$

Equation (6) is subsequently factored with respect to the DoFs, made dimensionless and can be found in Eq. (7)

$$\begin{aligned}\bar{\Phi}[\mathbf{u};\lambda;f_a;f_s] = &\frac{1}{2}\varphi_1^2(\alpha+1) + \frac{1}{2}\varphi_2^2(1+\beta) + 2\varphi_1\varphi_2 \\ &+\frac{1}{2}\omega\left[\lambda+\left(\varphi_1^2+\varphi_1\varphi_2+\varphi_2^2\right)\right]^2 \\ &+\varphi_1\left(\frac{1}{2}f_a\omega+\frac{1}{2}f_s\omega\right) - \frac{1}{2}f_s\omega\varphi_2\end{aligned} \tag{7}$$

$\bar{\Phi}$ denotes the dimensionless potential energy; parameters $\alpha = (k_a + 3k_b)/(k_b + k_c)$ and $\beta = (k_d + 3k_c)/(k_b + k_c)$ describe the stiffness ratios between the torsion springs in the linkage; $\omega = kL^2/(k_b + k_c)$ governs the dimensionless axial stiffness; $\lambda = d/L$ denotes the dimensionless pre-loading that is imposed; and $f = F/(kL)$ denotes the dimensionless imposed external load with F denoting F_a or F_s. The first step in solving the buckling problem helps to obtain the equilibrium equations by finding a stationary

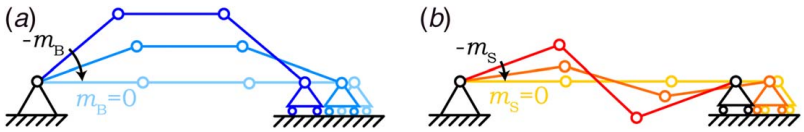

Fig. 4 Schematic representation of linkage deformation using the buckling modes (*a*) B and (*b*) S. From the buckled configuration, the modal amplitude is decreased until it reaches zero in the flat configuration.

value of the potential energy with respect to a kinematically admissible perturbation of the DoF $\delta\mathbf{u}$ using Eq. (8) [20,22]. The obtained equilibrium equations can be found in Eq. (9)

$$\delta\bar{\Phi} = \bar{\Phi}'\delta\mathbf{u} = \frac{\partial\bar{\Phi}}{\partial\varphi_1}\delta\varphi_1 + \frac{\partial\bar{\Phi}}{\partial\varphi_2}\delta\varphi_2 = 0 \tag{8}$$

$$\begin{cases} \dfrac{\partial\bar{\Phi}}{\partial\varphi_1} = \varphi_1(1+\alpha) + 2\varphi_2 + \omega\left[\lambda + \left(\varphi_1^2 + \varphi_1\varphi_2 + \varphi_2^2\right)\right](2\varphi_1 + \varphi_2) \\ \qquad + \dfrac{1}{2}f_a\omega + \dfrac{1}{2}f_s\omega = 0 \\ \dfrac{\partial\bar{\Phi}}{\partial\varphi_2} = 2\varphi_1 + \varphi_2(1+\beta) + \omega\left[\lambda + \left(\varphi_1^2 + \varphi_1\varphi_2 + \varphi_2^2\right)\right](\varphi_1 + 2\varphi_2) \\ \qquad - \dfrac{1}{2}f_s\omega = 0 \end{cases} \tag{9}$$

By solving the equilibrium equations in Eq. (9), the pre-buckling solution $\mathbf{u}_0 = [0, 0]^T$ for $\lambda \neq 0$ is obtained. This is a stable solution describing the state of the system prior to buckling for a pre-load λ increasing from zero, or the flat state from Fig. 1(*a*) in short. The critical buckling loads and corresponding modes are obtained by evaluating the stability of $\mathbf{u}_0$ using the buckling condition in Eq. (10) [22]. $\bar{\Phi}_c''$ denotes the second derivatives of the dimensionless potential energy evaluated at the pre-buckling solution $\mathbf{u}_0$ and the critical pre-load $\lambda = \lambda_c$, $\boldsymbol{\theta}$ denotes the buckling modes of the system. The buckling condition returns the generalized non-dimensional eigenvalue problem in Eq. (11). A trivial solution would be that $\boldsymbol{\theta} = \mathbf{0}$; however, this means that no buckling is occurring. Therefore, a non-trivial solution can only be found for a singular $\bar{\Phi}_c''$

$$\bar{\Phi}''[\mathbf{u}_0(\lambda_c);\lambda_c] = \bar{\Phi}_c''\boldsymbol{\theta}\delta\mathbf{u} = 0 \tag{10}$$

$$\bar{\Phi}_c''\boldsymbol{\theta} = \{A + \mu B\}\boldsymbol{\theta} = \mathbf{0} \quad \text{where } A = \begin{bmatrix} \alpha+1 & 2 \\ 2 & \beta+1 \end{bmatrix}, \quad B = \begin{bmatrix} 2 & 1 \\ 1 & 2 \end{bmatrix} \tag{11}$$

2.2.3 Critical Load Matching. Solving Eq. (11) by setting $C = B^{-1}A$ returns the eigenvalues $\mu_i = \lambda_i\omega$ and eigenvectors $\boldsymbol{\theta}_i$, which represent the dimensionless critical buckling loads and corresponding modes, respectively, for $i = 1, 2$. The lowest value of μ_i is the first critical buckling load μ_1 and the second lowest is the second critical buckling load μ_2. The CLR for the TSL is defined as the ratio μ_1/μ_2 and can be found in Eq. (12). It is found that the CLR becomes unity, i.e., the two buckling loads are exactly equal to each other, for $\alpha = \beta = 3$.

$$\frac{\mu_1}{\mu_2} = \frac{\alpha + \beta - \sqrt{\alpha^2 - \alpha\beta + \beta^2 - 3(\alpha+\beta) + 9}}{\alpha + \beta + \sqrt{\alpha^2 - \alpha\beta + \beta^2 - 3(\alpha+\beta) + 9}} \tag{12}$$

The CLR governs the values of the stiffness ratios α and β, and thus physically the relative stiffness of the torsion springs in the TSL. Hence, by varying the CLR, different linkage architectures are obtained. According to a unity CLR, α and β are constrained to $\alpha = \beta = \kappa$. Assuming symmetry in the TSL as $k_a = k_d = c^*$ and $k_b = k_c = c$, returns $k_a = k_d = 3c$ for $\kappa = 3$. Therefore, a unity CLR is obtained when the two grounded springs are three times stiffer relative to the two ungrounded springs. This architecture will be denoted as 3c-c-c-3c, in which c denotes the stiffness of the torsion springs and the hyphens denote the links between the springs. Four additional architectures $\kappa = \{2, 2.5, 3.5, 4\}$ are denoted as c-c-c-c, 2c-c-c-2c, 4c-c-c-4c, 5c-c-c-5c, respectively. To analyze the effect of the CLR on the mechanical behavior, the symmetric and asymmetric FD characteristics of these five architectures are determined by solving Eq. (9) for f_a and f_s, respectively, for a given displacement field.

2.2.4 Modal Analysis. The TSL has two DoFs describing the deflection and its two buckling modes B and S. Expressed in the DoFs, it holds that $\varphi_1 = -\varphi_2$ for the B-mode, and $\varphi_1 = \varphi_2$ for the S-mode [25]. Inversely, it holds that any configuration of the linkage may be decomposed in buckling modes B and S as found in Eq. (13). Here, the DoFs $\mathbf{u}$ are projected on a modal basis $\boldsymbol{\theta}$, obtained from Eq. (11), spanned by the buckling modes B and S. For a given linkage configuration, the modes are scaled with their modal amplitudes m_B and m_S. Modal amplitudes are linked to the displacement using mode participation χ. As opposed to the modal amplitude, which is solely the scaling of the mode, the participation represents the measure of contribution, e.g., $\chi_i = 1$ means that the linkage configuration is fully described by mode i, and it holds that $\sum_i^N \chi_i = 1$ [26].

$$\mathbf{u} = \begin{bmatrix} \varphi_1 \\ \varphi_2 \end{bmatrix} = \boldsymbol{\theta}\mathbf{m} = \begin{bmatrix} 1 & 1 \\ -1 & 1 \end{bmatrix}\begin{bmatrix} m_B \\ m_S \end{bmatrix} \quad \text{and} \quad \chi_i = \frac{|m_i|}{|m_B + m_S|} \tag{13}$$

The potential energy of the linkage under transversal deflection can be decomposed in strain energy contributions of the B and S-modes using this decomposition. The dimensionless strain energy $\bar{E}$ expressed in the modal basis can be found in Eq. (14). The strain energy contribution of each mode can be evaluated by scaling the modes separately and evaluating Eq. (14), which is schematically represented in Fig. 4.

$$\bar{E}[\mathbf{m};\alpha;\beta] = \frac{1}{2}m_B^2(\alpha+\beta-2) + \frac{1}{2}m_S^2(\alpha+\beta+6) + m_B m_S(\alpha-\beta) \tag{14}$$

2.3 Mechanical Design and Manufacturing. The TSL in Fig. 2 is converted into an equivalent lumped-compliant mechanism by replacing the torsion springs with flexures. In Fig. 5(*a*), the designed mechanism is depicted with the corresponding dimensions. It comprises three rigid links (1) of length B, width W and thickness H, and two clamping blocks. The left clamping block (2) is equivalent to grounded revolute joint of the TSL. The right clamping block (3) is equivalent to the slider joint, with two slots (4) allowing for a variable pre-loading displacement d. Two flexures (5), representing the grounded springs, of width w and thickness t connect the two outermost links to the clamping blocks, while two flexures (6), representing the ungrounded springs, of width w_f and thickness t interconnect the links. The flexures are clamped to the links using a bolt connection and a cap (7), creating a fixed-fixed boundary and a flexure length l. The assembly is mounted on a base plate (8). The links and the clamping blocks are milled from aluminum. The flexures are manufactured from 0.20 mm thick AISI 301 spring steel using a Spectra Physics Talon 355-15 diode pumped

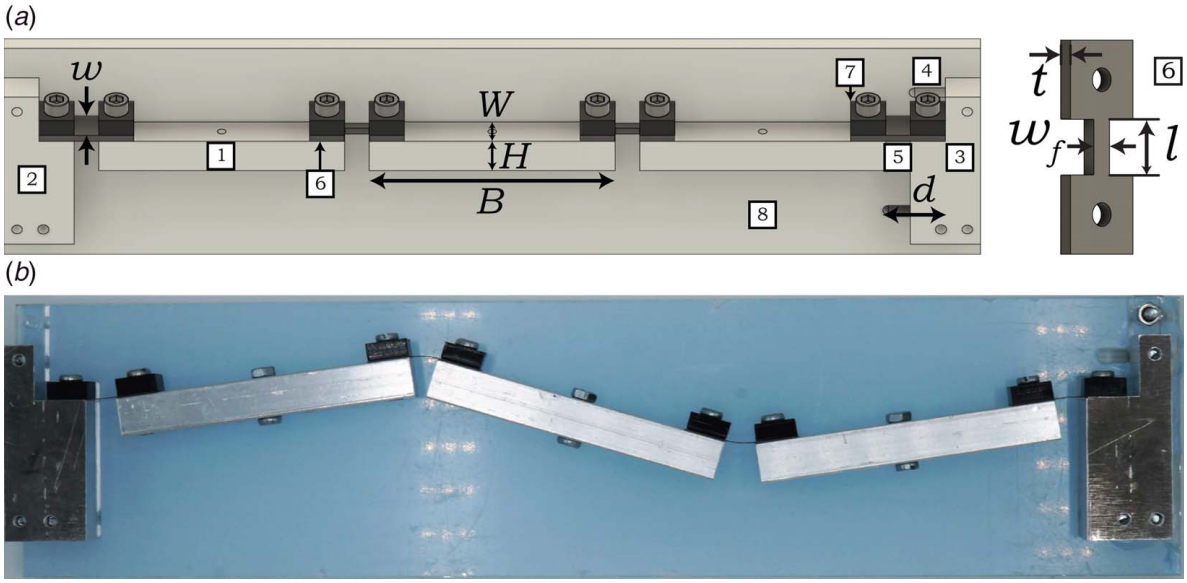

Fig. 5 Designed lumped-compliant four-bar mechanism: (*a*) schematic showing the design of the unloaded mechanism and ungrounded flexures with the dimensions indicated. The design comprises (1) rigid links, (2) grounded revolute joint, (3) slider joint, (4) with pre-loading slots, (5) grounded flexures, (6) ungrounded flexures with variable width, (7) PMMA caps, and (8) mounting base plate. (*b*) By applying a pre-load the manufactured mechanism may buckle into the S-mode.

Table 1 Relevant parameters of the manufactured lumped-compliant four-bar mechanisms

Fixed parameter	Symbol	Value (mm)
Link length	B	70
Link width	W	10
Link thickness	H	10
Grounded flexure width	w	10
Flexure thickness	t	0.20
Flexure length	l	7
Pre-load displacement	d	5
CFBM architecture	**Ungrounded flexure width w_f : [mm]**	
c-c-c-c	10	
2c-c-c-2c	5	
3c-c-c-3c	3.33	
4c-c-c-4c	2.50	
5c-c-c-5c	2	

solid-state (DPSS) UV laser cutter with a wavelength of 355 nm and a maximum power of 15 W at 50 kHz. The stiffness ratios κ from the five linkage architectures (Sec. 2.2.3) are achieved by varying the flexural rigidities of the ungrounded flexures relative to the grounded flexures. The flexural rigidity is determined as the product of torsion stiffness k_a, k_b, k_c, k_d and the flexure length [27]. For a constant flexure length and grounded flexure width, the rigidities for the ungrounded flexures (displayed in Fig. 5(*a*)) are governed by w_f. The post-buckled state, e.g., the S-mode displayed in Fig. 5(*b*), is obtained by inducing a pre-loading displacement $d = 5$ mm and fixing the slider joint (3), rendering the mechanism a lumped-compliant four-bar mechanism (CFBM) with one DoF. All parameters are summarized in Table 1.

2.4 Finite Element Modeling. To simulate the mechanical behavior of the post-buckled CFBM architectures, a finite element model was constructed in ANSYS Mechanical APDL. The flexures are modeled as linear elastic ($E = 190$ GPa, $\nu = 0.34$, $\rho =$

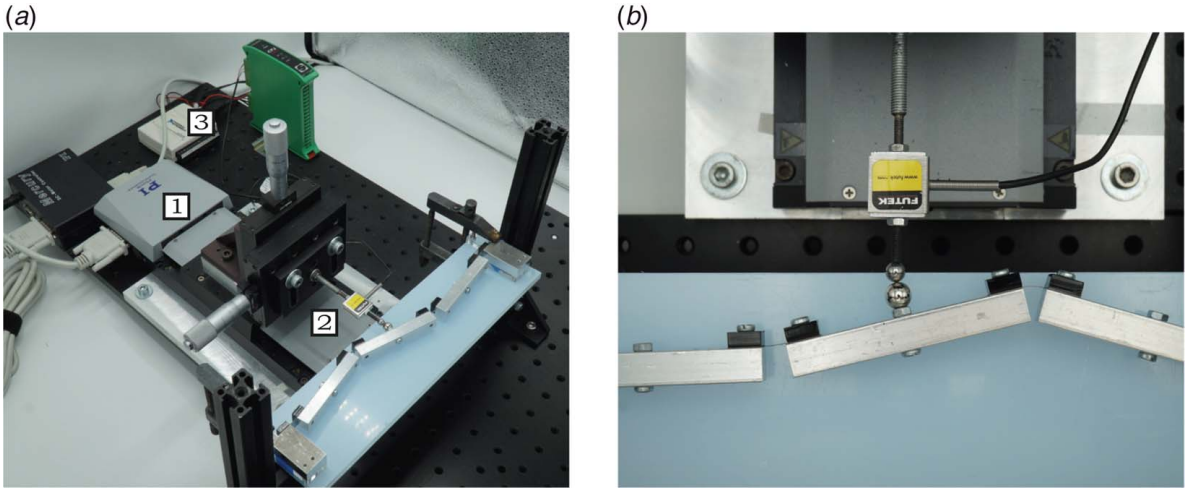

Fig. 6 Experimental setup for measuring force–deflection behavior. The used components (*a*) comprise (1) a PI M-505 motion stage, (2) a FUTEK LRM200 force sensor, and (3) an NI USB-6008 data acquisition unit. A rolling contact (*b*) ensures that contact between the sensor and the mechanism remains in the unstable motion region.

7890 kg/m^3) two-node Timoshenko beam elements (BEAM188). Linear buckling analysis is performed to determine the first two buckling loads and the corresponding modes of the CFBM. An initial imperfection is added to prevent crashing in the pre-loading phase due to singularities. The pre-loading displacement d is applied as described in Sec. 2.3, and subsequently, an incremental displacement is applied in either O_a or O_s while recording the reaction force to obtain the FD characteristics for asymmetric and symmetric actuation.

2.5 Experimental Setup. The FD characteristics of the mechanism architectures were evaluated experimentally with the setup shown in Fig. 6(*a*). To apply the desired displacement to the mechanism, a PI M-505 motion stage with an internal encoder for the displacement data is used. The force required for applying the displacement to the mechanism is measured by a FUTEK LRM200 force sensor. A rolling point contact between the mechanism and force sensor is established using a probe with a bearing ball attached to the sensor, and a spherical magnet attached to the mechanism, as shown in Fig. 6(*b*). The magnet ensures that contact remains in the unstable region. Data were recorded using an NI USB-6008 in 100 steps with a resolution of 750 μm.

3 Results

The analytical buckling loads and the CLR values are tabulated in Table 2 for the five TSL architectures.

The FD characteristics of the TSL and CFBM architectures are depicted in Figs. 7 and 8 for the symmetric and asymmetric actuation, respectively. The analytical results are compared to the finite element analysis (FEA) and experimental results. The chronology of deflection is presented in Figs. 9 and 10 for the symmetric and asymmetric actuation, respectively. The numerals are indicated in the c-c-c-c Architecture FD characteristics at the corresponding locations.

Table 2 Buckling loads P_B and P_S and CLR values for analytical analysis

Architecture	P_B:(N)	P_S:(N)	CLR(–)
c-c-c-c	4.77	7.96	0.60
2c-c-c-2c	3.58	4.38	0.82
3c-c-c-3c	3.18	3.18	1.00
4c-c-c-4c	2.98	2.59	0.87
5c-c-c-5c	2.86	2.23	0.78

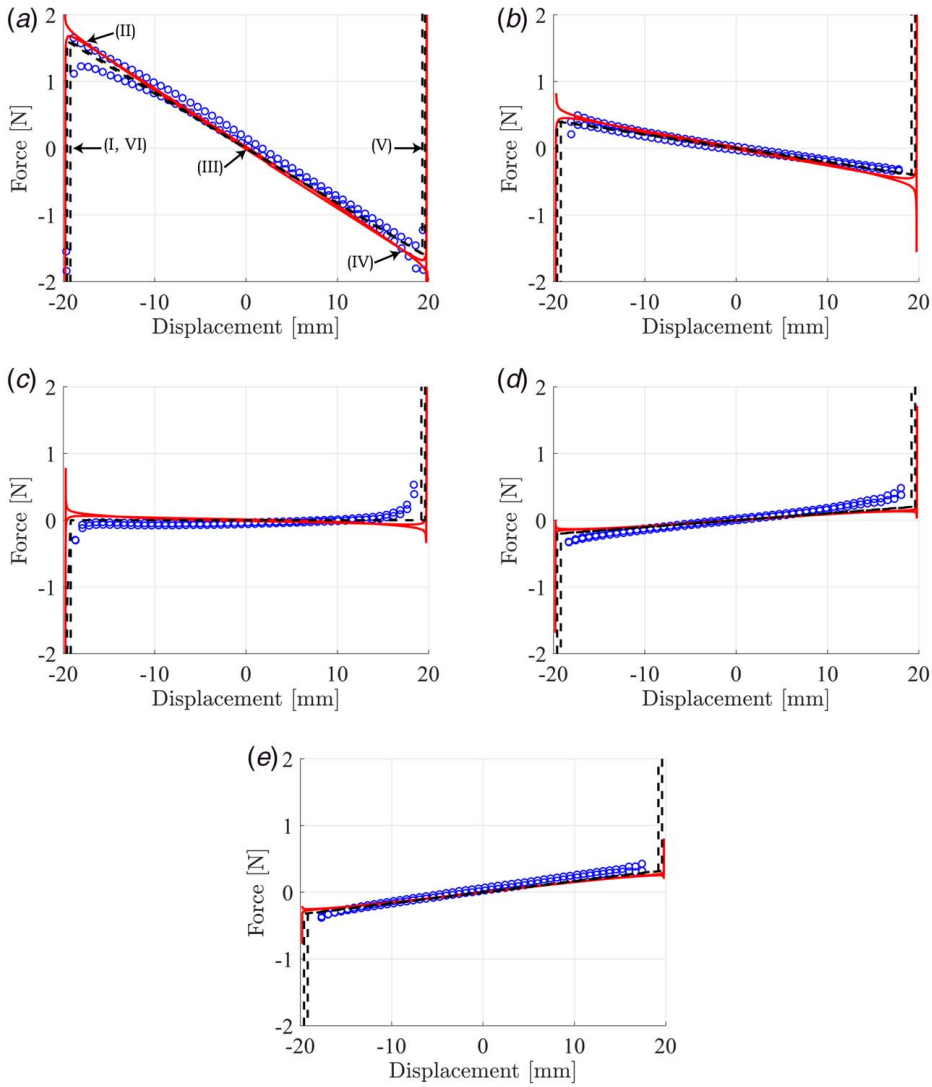

Fig. 7 Symmetric actuation: comparison of (--) analytical, (—) FEA, and (o) and experimental relation between actuation force F_s and displacement of actuation point O_s for pre-loading displacement $d = 5$ mm. Evaluated for five mechanism architectures: (*a*) c-c-c-c, (*b*) 2c-c-c-2c, (*c*) 3c-c-c-3c, (*d*) 4c-c-c-4c, and (*e*) 5c-c-c-5c. Numerals correspond to those in Fig. 9, indicating the chronology of deflection.

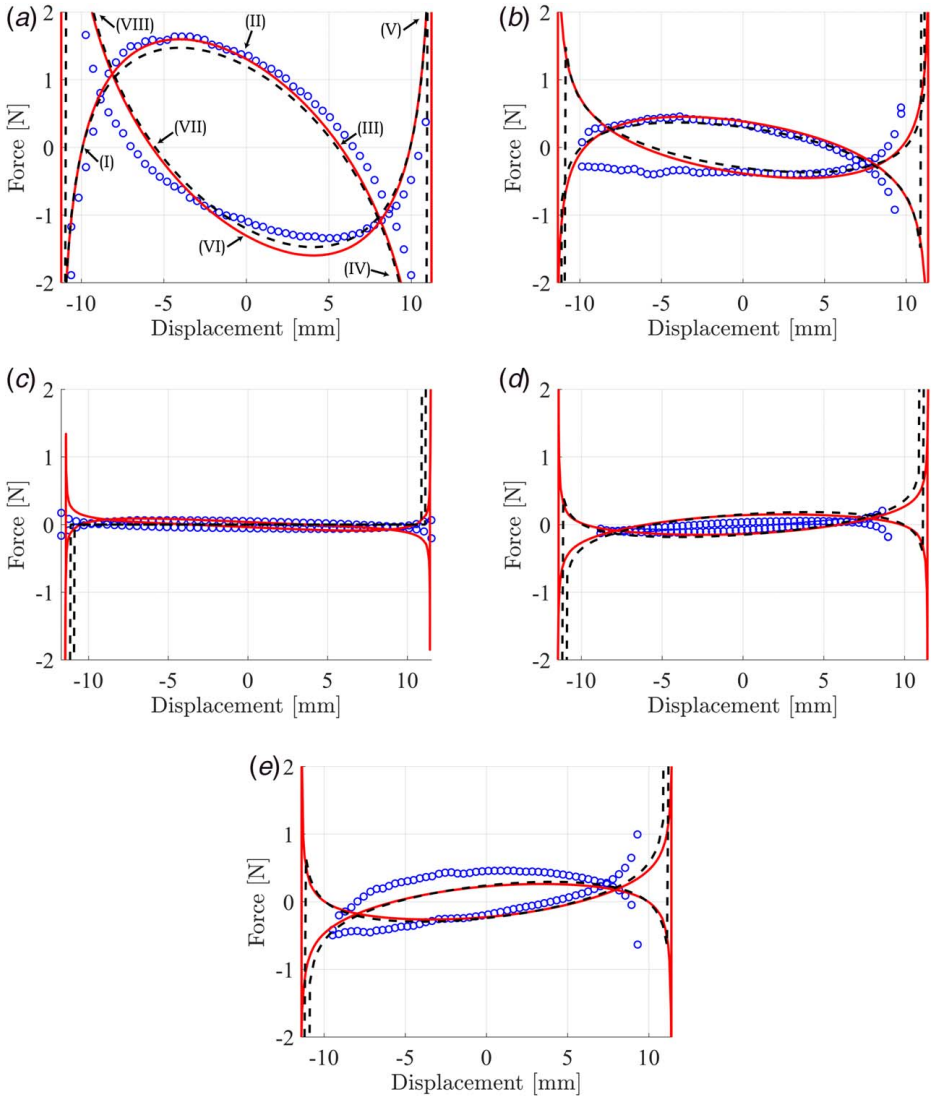

Fig. 8 Asymmetric actuation: comparison of (--) analytical, (—) FEA, and (o) and experimental relation between actuation force F_a and displacement of actuation point O_a for pre-loading displacement $d = 5$ mm. Evaluated for five mechanism architectures: (*a*) c-c-c-c, (*b*) 2c-c-c-2c, (*c*) 3c-c-c-3c, (*d*) 4c-c-c-4c, and (*e*) 5c-c-c-5c. Numerals correspond to those in Fig. 10, indicating the chronology of deflection.

Figure 11(*a*) depicts the relation between the mode participation of the B and S-modes and the vertical displacement of O_s under transversal deflection. In Figs. 11(*b*)– 11(*d*), the dimensionless strain energy of the two separate modes, obtained by evaluating Eq. (14), is plotted together with their sum for the 3c-c-c-3c, c-c-c-c, and 5c-c-c-5c Architectures for symmetric actuation. The numerals correspond to the chronology of deflection in Fig. 9

4 Discussion

4.1 Force–Deflection Characteristics of Architectures. In both actuation cases, the same effect is observed due to a change in κ: there is a counter-clockwise rotation of the FD characteristic parts between the ends as κ, i.e., the torsion stiffness ratios, increases. As the κ increases from the c-c-c-c Architecture to the 3c-c-c-3c, the stiffness gradually diminishes to zero. Looking into the CLR, it is observed that as the CLR approaches unity, the stiffness reduces. Static balancing is achieved in the mechanism as a result of matching the first two buckling loads, i.e., achieving a unity CLR value, in the 3c-c-c-3c Architecture. This strong reduction in stiffness matches the results found in Refs. [18,19], which provides further evidence that the CLR can be used as a method for stiffness compensation in compliant mechanisms. The simplicity of the TSL allowed for an insightful analysis of this method. To draw more general conclusions however, research regarding, e.g., designs with variable link lengths or more DoFs in the large deformation regime are required.

The change in sign of the FD slope for the 4c-c-c-4c and 5c-c-c-5c Architectures is ascribed to the buckling modes changing "order." Whereas the first buckling mode in the c-c-c-c Architecture is the B-mode, it becomes the S-mode for the 4c-c-c-4c and 5c-c-c-5c Architectures, which is observed in Table 2. Architectures c-c-c-c to 3c-c-c-3c have the B-mode as two stable positions on either side of the motion range. The S-mode has a single stable position at the middle of the motion range. This results in the mechanism acting as a spring with positive stiffness. The same counter-clockwise rotation of the FD characteristics is found in Ref. [28] for a Von Mises truss with a spring attached to the middle joint. For an increase in spring stiffness, the slope of the FD transitions from negative, to perfectly flat, to positive. Reference [29] obtained the same behavior for a Von Mises truss and denoted it as a zero-stiffness structure.

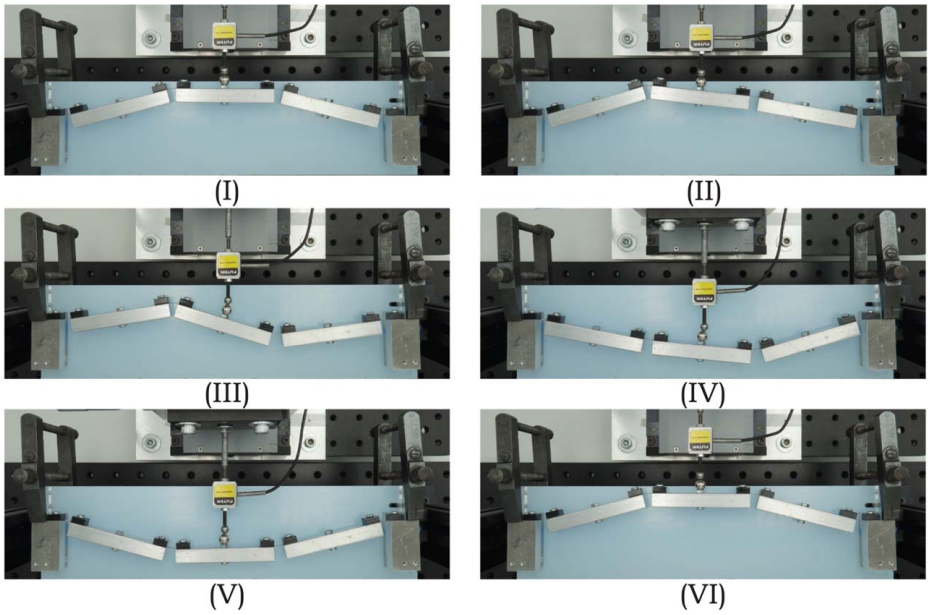

Fig. 9 Chronology of mechanism deflection for symmetric actuation (numerals refer to those in Fig. 7)

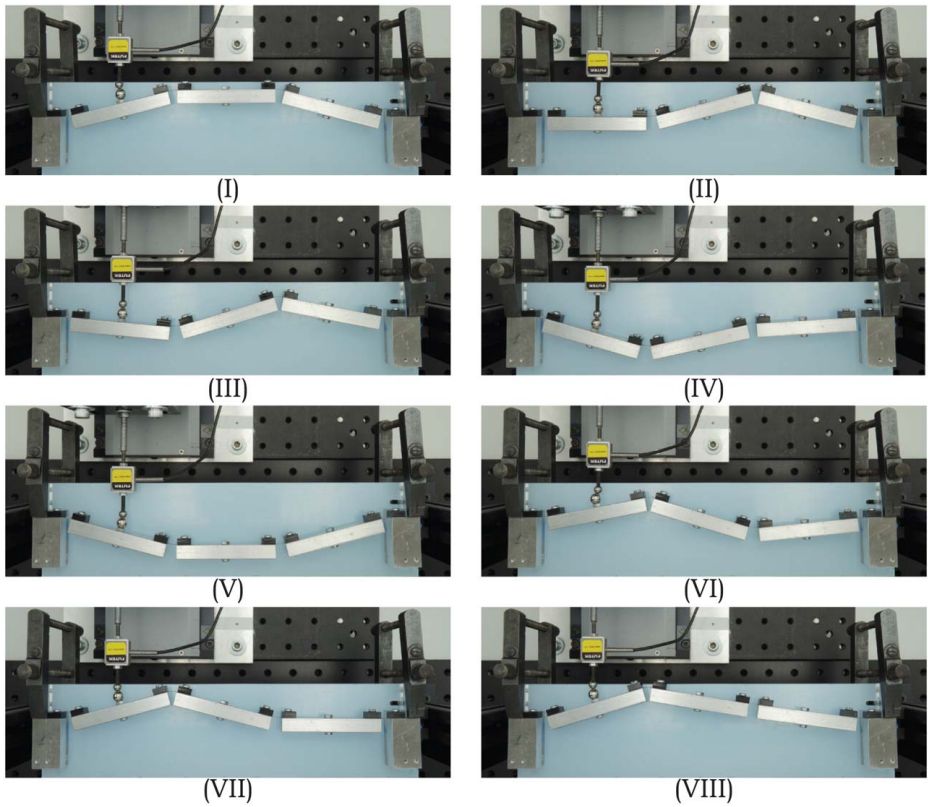

Fig. 10 Chronology of mechanism deflection for asymmetric actuation (numerals refer to those in Fig. 8)

The stiffness of the asymmetric FD characteristics may be approximated by taking the slope between the crossings of the loops, which is observed to follow the same trend as in the symmetric FD characteristics. It can also be observed that the area of the loops decreases as the 3c-c-c-3c Architecture is approached, matching the results in Ref. [19]. Reference [30] quantified the area under this loop as the energy required for deformation; hence, the energy decreases as we approach the 3c-c-c-3c Architecture.

4.2 Decomposition of the Strain Energy. From Fig. 11(*a*), it can be observed that the configuration of the linkage in the equilibria is fully defined by a single mode. The strain energy in the equilibria is thus equivalent to that of the corresponding buckling mode and determined by the pre-loading displacement and critical load, which corresponds to what was found in Ref. [19]. In the 3c-c-c-3c Architecture, the CLR is unity, and therefore the three equilibria have equal strain energy. As a result, it is observed that

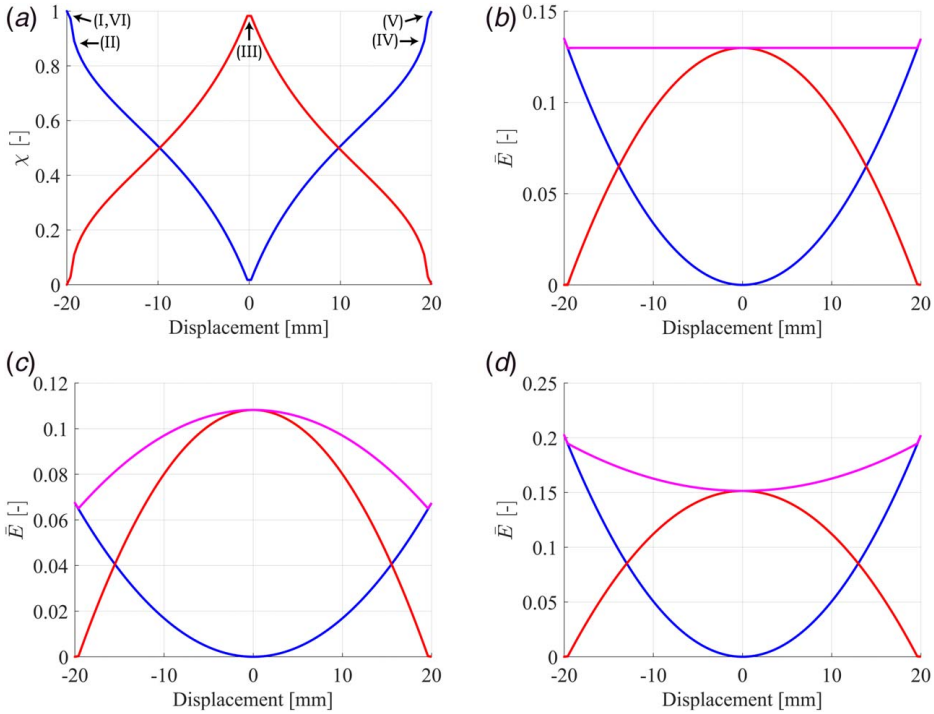

Fig. 11 (*a*) Relation between mode participation χ and displacement of symmetric actuation point O_s for (—) mode B, and (—) mode S. The numerals correspond to the chronology of deflection in Fig. 9, indicating the configuration of the linkage. (*b–d*) Dimensionless strain energy $\bar{E}$ for each mode is plotted separately together with the sum of both contributions (—) at a pre-loading displacement $d = 5$ mm for the (*b*) 3c-c-c-3c, (c) c-c-c-c, and (*d*) 5c-c-c-5c Architectures.

two strain energy contributions sum to a constant value throughout the motion range. The obtained constant strain energy results in zero actuation force during transversal deflection of the 3c-c-c-3c Architecture. Hence, it can be said that by obtaining a unity CLR, the mechanism is statically balanced between its equilibrium positions.

The counter-clockwise rotation observed in the FD characteristics due to change in the mode order is depicted by the strain energy as well. Two equilibrium positions, both described by the B-mode, which are separated by a barrier that is defined by the S-mode are found for the c-c-c-c Architecture (Fig. 11(*c*)). The downward opening parabola indicates that the c-c-c-c Architecture exhibits bistable behavior, as is observed in Fig. 7(*a*). A single minimum of strain energy for $\chi_S = 1$ is observed for the 5c-c-c-5c Architecture, meaning that the stable equilibrium is fully described by S-mode (Fig. 11(*d*)). The upward opening parabola indicates monostability, which is observed as the positive stiffness in Fig. 7(*e*).

4.3 Model Accuracy. From Figs. 7 and 8, it is observed that the analytical model and the experimental results comply well in terms of stiffness. The moderate rotations assumption introduces a slight error to the kinematics that remains within a 2% bound. In symmetric actuation of the 3c-c-c-3c Architecture, a discrepancy between the stiffness in the experimental and the analytical results is observed, which is ascribed to imperfections in the assembly process. These imperfections are included in the finite element model. Nevertheless, a discrepancy between the FEA and experimental results is still observed. This indicates the difficulty of achieving static balancing in practice due to the sensitivity of the buckling loads to manufacturing and assembly. From Fig. 10, it can be observed that the asymmetric actuation results in two load paths occurring. The shapes of the FD characteristics of the c-c-c-c Architecture match those found for symmetric and asymmetric actuation of a bistable buckled prismatic beam [31]. Therefore, it can be said that the proposed analytical model predicts the behavior of such a beam well.

5 Conclusion

In this paper, we have investigated the effect of matching the first two buckling loads on the force–deflection characteristics in a five-bar linkage. An analytical simply supported five-bar linkage model consisting of three rigid links; a prismatic slider joint with a linear spring capturing the buckling behavior; and four torsion springs in the revolute joints was proposed to achieve this. The buckling problem was solved, and it was found that the ratio between the buckling loads changes as a function of the torsion stiffness ratios in the linkage. The first two buckling loads are exactly equal when the two grounded springs are three times stiffer than the two ungrounded springs. The force–deflection characteristics of five linkage architectures with the torsion spring stiffness ratio ranging from 1 to 5 were evaluated analytically, numerically using finite element analysis, and experimentally. In the finite element and experimental models, the torsion springs were replaced by short flexures and the slider joint was fixed after pre-loading, creating a lumped-compliant four-bar mechanism. It was shown that by matching the first two buckling loads, the force required for deformation entirely diminishes, and static balancing is achieved. Using modal analysis, it was shown that the sum of the decomposed strain energy per buckling mode is constant throughout the motion range due to the matching buckling loads. This indicates that matching the first two buckling loads is a useful method in stiffness compensation or static balancing of buckled lumped-compliant four-bar mechanisms.

Conflict of Interest

There are no conflicts of interest.

Data Availability Statement

The authors attest that all data for this study are included in the paper.

References

[1] Herder, J. L., 2001, "Energy-Free Systems; Theory, Conception and Design of Statically Balanced Spring Mechanisms," Ph.D. thesis, Delft University of Technology, Delft, The Netherlands.

[2] Chen, G., and Zhang, S., 2011, "Fully-Compliant Statically-Balanced Mechanisms Without Prestressing Assembly: Concepts and Case Studies," Mech. Sci., **2**(2), pp. 169–174.

[3] Herder, J. L., 1998, "Design of Spring Force Compensation Systems," Mech. Mach. Theory., **33**(1–2), pp. 151–161.

[4] Deepak, S. R., and Ananthasuresh, G. K., 2012, "Static Balancing of a Four-Bar Linkage and Its Cognates," Mech. Mach. Theory., **48**(1), pp. 62–80.

[5] Deepak, S. R., and Ananthasuresh, G. K., 2012, "Perfect Static Balance of Linkages by Addition of Springs But Not Auxiliary Bodies," ASME J. Mech. Rob., **4**(2), p. 021014.

[6] Soethoudt, B., and Herder, J. L., 2007, "Synthesis of Perfect Spring Balancers With Higher-Order Zero-Free-Length Springs," Proceedings of the ASME 2007 International Design Engineering Technical Conferences and Computers and Information in Engineering Conference. Volume 8: 31st Mechanisms and Robotics Conference, Parts A and B, Las Vegas, NV, Sept. 4–7, pp. 751–762.

[7] Gallego, J. A., and Herder, J. L., 2010, "Criteria for the Static Balancing of Compliant Mechanisms," Proceedings of the ASME 2010 International Design Engineering Technical Conferences and Computers and Information in Engineering Conference. Volume 2: 34th Annual Mechanisms and Robotics Conference, Parts A and B, Montreal, Quebec, Canada, Aug. 15–18, pp. 465–473.

[8] Tolou, N., and Herder, J. L., 2009, "Concept and Modeling of a Statically Balanced Compliant Laparoscopic Grasper," Proceedings of the ASME 2009 International Design Engineering Technical Conferences and Computers and Information in Engineering Conference. Volume 7: 33rd Mechanisms and Robotics Conference, Parts A and B, San Diego, CA, Aug. 30–Sept. 2, pp. 163–170.

[9] Lamers, A., Gallego Sánchez, J. A., and Herder, J. L., 2015, "Design of a Statically Balanced Fully Compliant Grasper," Mech. Mach. Theory., **92**, pp. 230–239.

[10] Merriam, E. G., Colton, M., Magleby, S., and Howell, L. L., 2013, "The Design of a Fully Compliant Statically Balanced Mechanism," Proceedings of the ASME 2013 International Design Engineering Technical Conferences and Computers and Information in Engineering Conference. Volume 6A: 37th Mechanisms and Robotics Conference, Portland, OR, Aug. 4–7, p. V06AT07A035.

[11] Kuppens, P. R., Bessa, M. A., Herder, J. L., and Hopkins, J. B., 2021, "Compliant Mechanisms That Use Static Balancing to Achieve Dramatically Different States of Stiffness," ASME J. Mech. Rob., **13**(2), p. 021010.

[12] Deepak, S. R., Hansoge, A. N., and Ananthasuresh, G. K., 2016, "Application of Rigid-Body-Linkage Static Balancing Techniques to Reduce Actuation Effort in Compliant Mechanisms," ASME J. Mech. Rob., **8**(2), p. 021005.

[13] Tolou, N., Henneken, V. A., and Herder, J. L., 2010, "Statically Balanced Compliant Micro Mechanisms (SB-MEMS): Concepts and Simulation," Proceedings of the ASME 2010 International Design Engineering Technical Conferences and Computers and Information in Engineering Conference. Volume 2: 34th Annual Mechanisms and Robotics Conference, Parts A and B, Montreal, Quebec, Canada, Aug. 15–18, pp. 447–454.

[14] Tolou, N., Estevez, P., and Herder, J. L., 2011, "Collinear-Type Statically Balanced Compliant Micro Mechanism (SB-CMM): Experimental Comparison Between Pre-Curved and Straight Beams," Proceedings of the ASME 2011 International Design Engineering Technical Conferences and Computers and Information in Engineering Conference. Volume 6: 35th Mechanisms and Robotics Conference, Parts A and B, Washington, DC, Aug. 28–31, pp. 113–117.

[15] Tolman, K. A., Merriam, E. G., and Howell, L. L., 2016, "Compliant Constant-Force Linear-Motion Mechanism," Mech. Mach. Theory., **106**, pp. 68–79.

[16] Gallego Sánchez, J. A., and Herder, J. L., 2011, "Buckling as a New Perspective on Static Balancing of Mechanisms," 13th World Congress in Mechanisms and Machine Science, Guanajuato, Mexico, June 19–23, pp. 1–7.

[17] Morsch, F. M., and Herder, J. L., 2010, "Design of a Generic Zero Stiffness Compliant Joint," Proceedings of the ASME 2010 International Design Engineering Technical Conferences and Computers and Information in Engineering Conference. Volume 2: 34th Annual Mechanisms and Robotics Conference, Parts A and B, Montreal, Quebec, Canada, Aug. 15–18, pp. 427–435.

[18] Kuppens, P. R., Herder, J. L., and Tolou, N., 2019, "Permanent Stiffness Reduction by Thermal Oxidation of Silicon," J. Microelectromech. Syst., **28**(5), pp. 900–909.

[19] Blad, T., van Ostayen, R., and Tolou, N., 2021, "A Method for Tuning the Stiffness of Building Blocks for Statically Balanced Compliant Ortho-Planar Mechanisms," Mech. Mach. Theory., **162**, p. 104333.

[20] Gambhir, M. L., ed., 2004, *Stability Analysis and Design of Structures*, Springer, Berlin, pp. 1–10.

[21] Barbero, E. J., Dede, E. K., and Jones, S., 2000, "Experimental Verifcation of Buckling-Mode Interaction in Intermediate-Length Composite Columns," Int. J. Solids. Struct., **37**(29), pp. 3919–3934.

[22] Budiansky, B., 1974, "Theory of Buckling and Post-Buckling Behavior of Elastic Structures," Adv. Appl. Mech., **14**(1), pp. 1–65.

[23] Wang, C. M., Wang, C. Y., and Reddy, J., 2015, *Exact Solutions for Buckling of Structural Members*, J. N. Reddy, ed., CRC Press, Boca Raton, FL, pp. 1–5.

[24] Timoshenko, S. P., and Gere, J. M., 1962, *Theory of Elastic Stability*, J. M. Gere, ed., 2n ed., Vol. 29, McGraw-Hill, Mineola, NY, pp. 46–106.

[25] Alfutov, N. A., 2000, "Basic Theory of Elastic Stability," *Stability of Elastic Structures*, Babitsky, V. I., and Wittenburg, J., eds., Foundations of Engineering Mechanics. Springer, Berlin, pp. 1–44.

[26] Cai, J., and Moen, C. D., 2015, "Automated Buckling Mode Identification of Thin-Walled Structures From 3D Finite Element Mode Shapes or Point Clouds," Proceedings of the Annual Stability Conference Structural Stability Research Council, Nashville, TN, Mar. 24–27, pp. 1–18.

[27] Lusk, C., 2013, "Using Pseudo-Rigid Body Models," *Handbook of Compliant Mechanisms*, Howell, L. L., Magleby, S. P., and Olsen, B. M., eds., Vol. 5., John Wiley & Sons, Inc., Hoboken, NJ, pp. 55–76.

[28] Schranz, C., Krenn, B., and Mang, H. A., 2006, "Conversion From Imperfection-Sensitive Into Imperfection-Insensitive Elastic Structures. II: Numerical Investigation," Comput. Methods. Appl. Mech. Eng., **195**(13–16), pp. 1458–1479.

[29] Tarnai, T., 2003, "Zero Stiffness Elastic Structures," Int. J. Mech. Sci., **45**(3), pp. 425–431.

[30] Cazottes, P., Fernandes, A., Pouget, J., and Hafez, M., 2009, "Bistable Buckled Beam: Modeling of Actuating Force and Experimental Validations," ASME J. Mech. Des., **131**(10), p. 101001.

[31] Camescasse, B., Fernandes, A., and Pouget, J., 2014, "Bistable Buckled Beam and Force Actuation: Experimental Validations," Int. J. Solids. Struct., **51**(9), pp. 1750–1757.